

Understanding the Molecular Weight Dependence of χ and the Effect of Dispersity on Polymer Blend Phase Diagrams

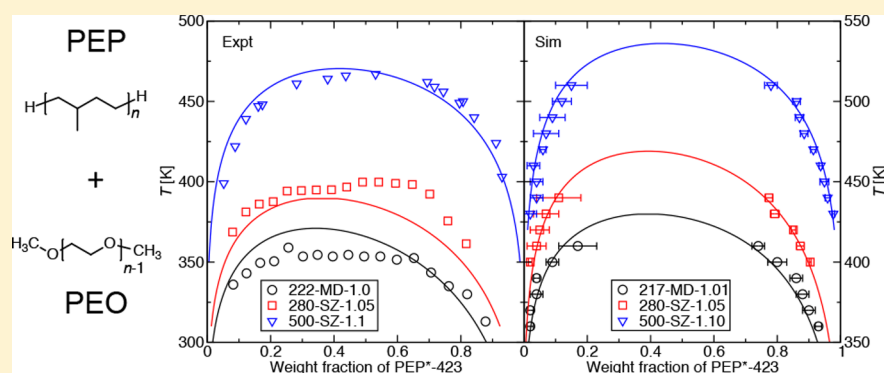
Qile P. Chen,^{†,‡,§} Shuyi Xie,[‡] Reza Foudazi,^{||} Timothy P. Lodge,^{*,†,‡} and J. Ilja Siepmann^{*,†,‡,§}

[†]Department of Chemical Engineering and Materials Science, University of Minnesota, 421 Washington Avenue SE, Minneapolis, Minnesota 55455-0132, United States

[‡]Department of Chemistry and [§]Chemical Theory Center, University of Minnesota, 207 Pleasant Street SE, Minneapolis, Minnesota 55455-0431, United States

^{||}Department of Chemical and Materials Engineering, New Mexico State University, MSC 3805, P.O. Box 30001, Las Cruces, New Mexico 88003-8001, United States

Supporting Information



ABSTRACT: Gibbs ensemble Monte Carlo simulations and cloud point measurements were performed to understand the molecular weight dependence of χ and the effect of dispersity on the phase behavior of polymer mixtures. Oligomeric blends consisting of poly(ethylene-*alt*-propylene) (PEP) and poly(ethylene oxide) dimethyl ether (PEO) were used as the model systems. First, the molecular weight dependence of χ for PEP/PEO mixtures was studied using simulations and experiments for PEP/PEO mixtures with various molecular weights. An empirical model with a single adjustable parameter k_{ij} is used to quantify this molecular weight dependence, and it allows for the accurate prediction of χ of PEP/PEO mixtures with arbitrary molecular weights. Second, the effects of molecular weight distribution (MWD) and dispersity (\mathcal{D}) of PEO on the PEP/PEO phase diagram were investigated via both simulations and experiments. When PEO is relatively monodisperse ($\mathcal{D} < 1.2$), the phase diagram is found to be insensitive to either MWD or \mathcal{D} , despite differentiation in molecular partitioning observed from simulations. However, the coexistence curve for mixtures containing PEO with a bimodal distribution and a large dispersity ($\mathcal{D} = 1.76$) differs dramatically from that for mixtures containing low-dispersity PEO, which suggests that the former mixture can no longer be treated as a binary system. Furthermore, structural analysis was performed from simulation trajectories to probe microscopic heterogeneity and aggregation behavior in the liquid phases. The results in this work permit the accurate prediction of χ and the phase diagram of disperse binary polymeric mixtures.

INTRODUCTION

The ability to engineer diverse polymers on the molecular level enables the creation of materials with a wide range of properties. Polymer blends, a soft matter analogue of alloys, provide a means to access materials properties that are beyond the reach of single-component polymeric materials.^{1–4} Knowledge of how the interactions between unlike segments influence the phase behavior is the key to the custom tailoring of desired polymeric materials properties. Flory–Huggins (FH) theory^{5,6} is widely used to correlate the mixture phase behavior with a binary interaction parameter χ :

$$\frac{\Delta G_m}{k_B T} = \frac{\phi_1}{N_1} \ln(\phi_1) + \frac{1 - \phi_1}{N_2} \ln(1 - \phi_1) + \chi(N_1, N_2, T) \phi_1(1 - \phi_1) \quad (1)$$

where ΔG_m is the free energy of mixing per reference site; k_B and T are the Boltzmann constant and the absolute temperature, respectively; N_i ($i = 1, 2$) is the ratio between molar volume of component i and the reference volume; and

Received: March 20, 2018

Revised: April 21, 2018

Published: May 9, 2018

ϕ_1 is the volume fraction of component 1. Experimentally, χ is typically fitted either to the binodal curve^{7,8} using eq 1 (denoted as χ_{eff}) or to the structure factor from neutron scattering experiments⁹ using the random-phase approximation¹⁰ (denoted as χ_{SANS}).

From eq 1, the accurate determination of χ is central to predicting the polymer blend phase diagram. In addition to theoretical advances,^{11–13} breakthroughs in computational method development enable a drive toward predicting χ from the molecular structures of polymers. One method is to perform molecular simulations on miscible binary blends, compute the structure factor, and then fit χ using the random-phase approximation, which mimics how χ_{SANS} is determined from neutron experiments.^{14,15} Another approach is to obtain χ through interfacial concentration profiles from immiscible binary blend simulations.^{16,17} In contrast to the above two methods where substantial assumptions are introduced in the calculation, we utilized vapor–liquid equilibria simulations to compute χ from the chemical potential in our earlier work¹⁸ (denoted as χ_{CP}). Recently, Zhang et al. developed a new method to compute χ by performing thermodynamic integration on the path along which one polymer transforms into the other.¹⁹

Despite this progress, two major questions still remain on how the coupling of eq 1 and the χ calculation method can be used to achieve the prediction of phase diagrams for binary polymeric mixtures. The first problem concerns the molecular weight dependence of χ . Since χ is often calculated for one specific set of molecular weights, it is important to know its molecular weight dependence in order to extrapolate χ to the molecular weights of interests. Unfortunately, the exact functional form of $\chi(N_1, N_2)$ for polymer blends is still a matter of discussion. For example, Han et al. studied polystyrene/poly(vinyl methyl ether) blends and concluded that χ_{SANS} for three sets of molecular weights that vary by about a factor of 3 are indistinguishable.²⁰ In contrast, Nedoma et al. reported that for polyisobutylene/(deuterated polybutadiene) blends $\chi_{\text{SANS}} \sim 1/N_{\text{AVE}}$, where $N_{\text{AVE}} = 4(N_1^{-1/2} + N_2^{-1/2})^{-2}$.^{21,22} A similar dependence of $\chi(N) \sim N^{-1}$ is also observed for symmetric diblock copolymers.²³ A theoretical study by Morse and Chung predicted a $\chi \sim N^{-1/2}$ dependence for polymer “mixtures” with $\chi \approx 0$. They attributed this relationship to the enhanced intrachain interactions as the chain length increases and thus the screening of the interchain interactions that contribute to χ .²⁴ In addition to the findings above, it is also intriguing whether the molecular weight dependence of χ implies the failure of the FH theory, since χ is a molecular-level parameter and should be independent of chain length.²⁵

The second problem is whether eq 1 is sufficiently accurate for a disperse “binary” mixture (i.e., a quasi-binary mixture), where molecular weight distribution (MWD) and dispersity (\mathcal{D}) might also play a role. Experimental phase diagrams of disperse polystyrene in methylcyclohexane show that coexistence curves for different total compositions do not collapse on one another, and the coexistence curves of disperse samples deviate by a few Kelvin from those of the relatively monodisperse ones.^{26,27} For a bimodal polymer distribution when the chain length ratio between the two polymer species is sufficiently large, the solution can phase-separate into three coexisting liquid phases near the critical point.^{28–30} Such deviations from binary mixture phase behavior motivate theoretical developments to understand the effect of dispersity. The standard approach is to apply continuous thermodynamics

to the FH theory to calculate the cloud point curve of the quasi-binary mixture.^{31–38} In addition, the partitioning of different molecular weight species between coexisting phases is identified by both experimental^{39,40} and theoretical^{34,38,41,42} studies.

The key barrier in studying these two problems is the limited molecular weight range, MWD, and \mathcal{D} accessible via experiments. On the one hand, a wide range of molecular weights is essential to provide sufficient precision in the determination of $\chi(N)$. On the other hand, however, the molecular weight range is restricted by the narrow temperature window for scattering or phase diagram measurements, which is limited between the glass transition temperature and the degradation temperature of polymers. Similarly, for the effects of MWD and \mathcal{D} , it is challenging to prepare polymer samples with the desired MWD and \mathcal{D} to achieve statistically meaningful conclusions.

Molecular simulations provide a convenient route to overcome the two problems mentioned above. First, simulations can access a much broader range of temperature without degradation. Second, both MWD and \mathcal{D} can be tuned with relative ease in the simulations. Third, simulations can directly access compositional and structural information that is difficult to extract from experiments, which can shed light on the molecular origin of the phase behavior.

Despite these advantages, direct simulations of polymer mixture phase behavior are rare, primarily due to the sampling difficulty of molecular transfers between two phases (needed for the computation of χ as well as the phase diagram). For example, the effect of dispersity on phase equilibria has only been simulated for Lennard-Jones particles.^{43–45} Fortunately, a variety of sampling techniques have been developed to assist the transfer of large molecules in order to realize the routine application of polymer (oligomer) phase equilibria simulations.^{46–58} In addition to the sampling difficulty, another challenge is the high sensitivity of the phase diagram to the free energy of transfer that governs the phase separation, which poses a stringent test on the accuracy of the molecular model used in the simulations. As shown in a recent example of the alkane/alkanol mixture phase diagram,⁵⁸ a difference of 1 kJ/mol in the transfer free energy, often regarded as a “small” deviation in force field development, results in about 50 K deviation in the coexistence curve.

In this work, Gibbs ensemble Monte Carlo (GEMC) simulations^{59,60} with advanced sampling techniques in conjunction with experimental cloud point measurements are utilized to study the phase behavior of model mixtures consisting of oligomeric poly(ethylene-*alt*-propylene) (PEP) and poly(ethylene oxide) dimethyl ether (PEO). Figure 1

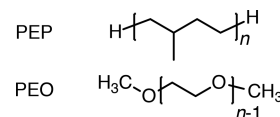


Figure 1. Repeat unit structures of PEP and PEO oligomers studied in this work.

shows the repeat unit structures of the two molecules. This incompatible mixture is selected as the model system because of the relatively low molar mass ($n < 10$) needed to demix the blend at room temperature, which permits the determination of phase diagrams by both simulations and cloud point measurements. In this paper, we first present results from simulations and experiments regarding χ of PEP/PEO mixtures with

various molecular weights, from which the molecular weight dependence of χ is identified and rationalized. In the second part, coexistence curves and cloud point curves for quasi-binary mixtures consisting of monodisperse PEP and polydisperse PEO are presented. The MWD and \mathcal{D} of PEO are varied, but the same M_n of 500 Da is maintained to understand the effects of MWD and \mathcal{D} on the phase diagram. Further analysis on the partitioning of different molecular weight PEO molecules and structures of the liquid in the two coexisting phases provides additional insight into the phase behavior of this mixture.

METHODS

Nomenclature. A range of PEP and PEO chain lengths are studied to explore the molecular weight dependence of χ , and they are denoted as [molecule]-[M_n]-[MWD]-[\mathcal{D}], in which M_n is the number-average molecular weight. MWD and \mathcal{D} in the nomenclature may be omitted if the sample is monodisperse. The MWD studied includes “MD” (monodisperse), “BM” (bimodal), and “SZ” (Schulz–Zimm).⁶¹ For example, PEO-222 indicates monodisperse oligomer PEO with five repeat units ($n = 5$), while PEO-500-SZ-1.10 represents disperse PEO with an M_n of 500 Da, a Schulz–Zimm MWD, and a dispersity of 1.10. The number of repeat units n , as defined in Figure 1, is also used to indicate the chain length of PEP and PEO. The molecular weight information on PEO used in experiments and simulations can be found in Table 1 and Figure 2, respectively. Note that PEP*-423 in

Table 1. Characterization of PEP and PEO Molecules Used in the Experiments

nomenclature	M_n [Da]	MWD	\mathcal{D}	note
PEP*-423	423 ^a	monodisperse	1.0 ^a	identical to squalane
PEO-222-MD-1.0	222 ^b	monodisperse ^b	1.0 ^b	
PEO-280-SZ-1.05	280 ^{c,d}	Schulz–Zimm ^d	1.05 ^d	
PEO-500-SZ-1.1	500 ^e	Schulz–Zimm ^e	1.1 ^e	
PEO-500-BM-1.1	500 ^f	bimodal	1.1 ^f	1:9 mole ratio of PEO-222-MD-1.0 and PEO-550-SZ-1.03

^aFrom supplier. ^bFrom Xie and Lodge.⁸ ^cFrom ¹H NMR. ^dFrom MALDI-MS. ^eFrom Washburn et al.⁶² ^fFrom theoretical calculations.

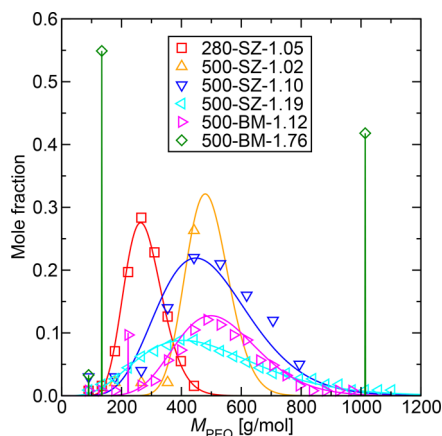


Figure 2. Molecular weight distribution of disperse PEO samples used in the simulations. Symbols represent simulation data, and lines are the Schulz–Zimm or bimodal distribution fit to the symbols.

this work refers to squalane (2,6,10,15,19,23-hexamethyltetracosane, similar to PEP-423 except for a head-to-head connectivity between the two middle segments), which has been used because of its high purity.

Experimental Details. Three PEO samples with different number-average molecular weights ($M_n = 222, 280, \text{ and } 530 \text{ Da}$) and squalane (PEP*-423) were purchased from the Sigma-Aldrich Corporation. The polymers were dried under dynamic vacuum for 48 h and then stored under vacuum. M_n and MWD of the PEO samples were assessed by matrix-assisted laser desorption/ionization mass spectroscopy (MALDI-MS) and ¹H NMR spectroscopy, and the results are provided in Figures S1–S7. The sample preparation and the cloud point measurements were performed following the protocol as used in earlier works.^{7,8}

Simulation Details. All the simulations were performed using the in-house Monte Carlo (MC) simulation software package MCCC-S-MN (Monte Carlo for Complex Chemical Systems–Minnesota).⁶³ GEMC simulations^{59,60} in the canonical (NVT) or isobaric–isothermal (NpT) ensemble were used to simulate the vapor–liquid equilibria (VLE) of single-component oligomers and their binary mixtures. For single-component oligomer simulations, 300 molecules were used for PEO-266 ($n = 6$), and 400 molecules were used for other oligomers. For binary mixtures, the PEP weight fraction was around 50%, and the system sizes were varied to allow for at least 10% of each molecule type in the vapor phase and a total system size of no smaller than 3000 interaction sites. The detailed system sizes for each system are listed in Table S1. A similar simulation protocol was used as described in our earlier paper.¹⁸ In brief, all the molecules were placed in the liquid phase during the initialization of the system. Center-of-mass translations, center-of-mass rotations, conformational moves,⁶⁴ volume exchange moves, and particle transfer moves were used to sample the configurational phase space of the system. In order to aid the molecular transfer between the vapor and the liquid phases, impurity molecules of shorter PEP or PEO oligomers (two molecules each) were also used, together with the interbox identity switch moves.^{65,66} This approach boosts the acceptance of transfer moves^{66,67} without sacrificing the accuracy, if proper corrections are applied ($\mathcal{D} < 1.01$).¹⁸

All VLE simulations were equilibrated for around 1.5×10^5 MC cycles (MCCs, consisting of N randomly selected moves, where N is the total number of molecules) until there was no drift in energies and number densities of each molecule in both phases. Then, simulations were run for at least another 3×10^5 MCCs as the production stage. The k -d tree data structure was used to accelerate unary PEP simulations.⁶⁸ Single-component thermodynamic properties such as liquid densities (ρ), vapor pressures (p_{vap}), cohesive energy densities (Π_{CED}), and solubility parameters (δ), as well as the χ parameters for binary mixtures, were extracted from these simulations as described in our previous work.¹⁸ In particular, Π_{CED} and δ were calculated using the following equation:

$$\delta = \sqrt{\Pi_{\text{CED}}} = \sqrt{\frac{U_{\text{vap}} - U_{\text{liq}}}{V_{\text{liq}}}} \quad (2)$$

where U_{vap} is the molar internal energy of the molecule in the vapor phase, U_{liq} is the molar internal energy of the liquid phase, and V_{liq} is the molar volume of the liquid phase.

In addition, liquid–liquid equilibria (LLE) of PEP*-423/PEO mixtures were simulated via NpT -GEMC simulations ($p = 1 \text{ bar}$). A three-box setup was used, in which two simulation boxes were used to represent two coexisting liquid phases while the third simulation box was used as the transfer medium.⁶⁹ A total of about 120 PEP molecules and more than 100 PEO molecules of various molecular weights (see Table S2) were used in the simulations, which led to 40–60% overall PEP weight fraction. The same types of moves as used in the VLE simulations were also applied to the LLE simulations. In addition, self-adapting fixed-end-point configurational-bias Monte Carlo (SAFE-CBMC) moves⁷⁰ were applied to PEO molecules when $n_{\text{PEO}} \geq 10$ to ensure good sampling of the internal conformation of these long-chain molecules. Furthermore, shorter oligomeric PEP molecules were used as impurities (e.g., $n_{\text{PEP}} = 1$ –5). This resulted in a

dispersity of 1.04 for PEP*-423. Impurities were also used for PEO, but they were included in the MWD and the calculation of \bar{D} . Similar to VLE simulations, direct particle transfer moves were only used for the shortest oligomers (i.e., PEP-72 and PEO-90), and the transfer of higher molecular weight molecules was achieved via the interbox identity switch moves, which were applied to all the neighboring molecular weight oligomer pairs (e.g., PEP-72 and PEP-142). The free energy of molecular transfer to and from the vapor phase was biased to ensure that there are on average 0.5–1.5 molecules for each PEP impurity molecule and 0.2–1.5 molecules for each PEO molecule in the vapor phase. Such bias does not affect the resulting liquid–liquid phase diagram because the same biasing potential is applied to both liquid–vapor box pairs, and its net effect on the liquid–liquid free energy of transfer is thus zero.⁵⁸ PEO molecules with $n \geq 19$ were not allowed to transfer to the PEP-rich liquid box or the vapor box because of their negligible solubilities in the alkane phase even at the highest temperature studied (the weight fraction of PEO-839 in PEP*-423 is less than 1% at $T = 510$ K). Similar to VLE simulations, all the systems were initialized with all the PEP molecules in one liquid box and all the PEO molecules in the other liquid box. These LLE simulations were equilibrated for at least 2×10^6 MCCs until there was no drift in energies or compositions for each phase, and the production lasted for at least another 5×10^5 MCCs.

Eight and 16 independent simulations were performed for VLE and LLE simulations, respectively. Statistical uncertainties of the simulation data were estimated from these uncorrelated runs and are reported as the 95% confidence interval. Similarly, uncertainties in experimental cloud point measurements are estimated from either the 95% confidence interval from three independent runs or the instrument error (± 1 K), whichever is greater.

Molecular Models. The TraPPE–UA (transferable potentials for phase equilibria–united atom) force field^{64,71,72} was used to model alkanes and ethers investigated in this study. The force field treats these molecules as pseudoatoms connected by the prescribed bond length, and bending angles and dihedral angles are allowed to vary. One CH_x ($x = 1, 2,$ and 3) group or one oxygen atom is described as one pseudoatom. The Lennard-Jones (LJ) 12–6 potential with the Lorentz–Berthelot combining rule⁷³ and the Coulomb potential for partial charges on the oxygen and α -carbon sites were used to model the interactions between two pseudoatoms. A spherical cutoff r_{cut} of 14 Å was used, and the interactions beyond the truncation distance were accounted for via analytical tail corrections.⁷⁴ The Ewald summation method⁶⁹ with a screening parameter of $\kappa = 3.2/r_{\text{cut}}$ and $K_{\text{max}} = \text{int}(\kappa L_{\text{box}}) + 1$ (L_i is the box length) was used to calculate the Coulomb interactions in the simulations involving PEO molecules.

In addition, we modified the TraPPE–UA ether force field to model the interactions between PEP and PEO more accurately. The original TraPPE–UA force field⁷² can reproduce the single-component properties of PEO oligomers (see Table S3 for the computed vapor–liquid equilibria data for an ether dimer, 1,2-dimethoxyethane, or PEO-90 from our nomenclature), but it fails to accurately predict χ for the binary alkane/ether mixture. As shown in Figure 3, the χ parameter of the *n*-dodecane/PEO-178 mixture is overestimated by more than 75% over the entire composition range, which implies that the binary interaction between alkane and ether is too unfavorable. The overestimation can be remedied by reducing the partial charges on the PEO atoms and adjusting the LJ parameters of the oxygen atom (i.e., rebalancing the dispersive and Coulomb contributions to the cohesive energy of PEO molecules). Since ether molecules can interact with alkane molecules through dispersive interactions but not dipole interactions in this nonpolarizable model, this approach can result in more favorable alkane–ether interactions and, equivalently, a smaller χ . Similarly, other literature findings also suggest that reducing the partial charges on the TraPPE–UA ether molecules enables more accurate prediction of the ether–water phase diagram⁵⁷ and Kovats retention indices for alkanols in PEO-type stationary phases.⁷⁵ Therefore, we modified the TraPPE–UA ether force field by scaling down the partial charges on the ether molecules and adjusting the LJ parameters of the oxygen atom. Several values of the oxygen partial charge were attempted between the original $-0.50 e$ and $-0.44 e$. This

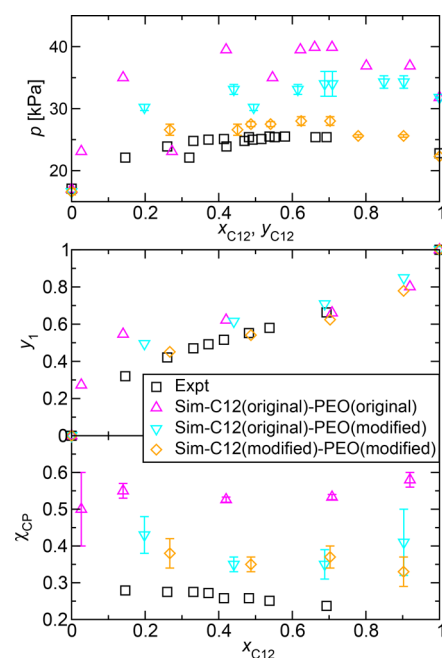


Figure 3. Vapor–liquid phase diagram (top), vapor composition as a function of liquid composition, i.e., separation factor (middle), and χ parameter (0.1 nm^3 is used as the reference volume) as a function of liquid composition for the binary mixture of *n*-dodecane (denoted as “C12”) and triethylene glycol dimethyl ether (denoted as “PEO”). The data are from different force field combinations, and we refer readers to the text for more details. Experimental data are taken from Treszczanowicz and Cieřlak.⁷⁶

range was selected because an earlier study suggested that a charge value around $-0.45 e$ is optimal for ether–water interactions.⁵⁷ The partial charge on the oxygen atom determines the partial charge on the α -carbon atoms to maintain the charge neutrality of the molecule. In addition, the LJ parameters of the oxygen atom were also tuned to reproduce single-component thermodynamic properties such as liquid densities, vapor pressures, and the critical point of a representative ether molecule, namely PEO-90. For each partial charge value, χ_{CP} for *n*-dodecane/PEO-178 mixtures was computed to allow for the selection of an optimal partial charge value.

It was found that χ_{CP} for the *n*-dodecane/PEO-178 mixture decreases with decreasing partial charge on the oxygen atom, and $q_{\text{O}} = -0.44 e$ worked best for this system among the partial charge values we selected (see Figure S10 for all the data with various partial charge values). The LJ parameters used for this partial charge are $\epsilon/k_{\text{B}} = 65$ K and $\sigma = 2.90$ Å (Table 2), and the corresponding single-component

Table 2. Nonbonded LJ Parameters and Partial Charges of the Modified PEO Force Field

atom type	ϵ/k_{B} [K]	σ [Å]	q [e]
CH_3	98	3.75	0.22
CH_2	46	3.95	0.22
O	65	2.90	-0.44

and binary VLE data are shown in Table S3 and Figure 3, respectively. Note that much smaller statistical uncertainties for the original ether force field data set (in magenta) are due to a much longer simulation trajectory. Indeed, one can see from Figure 3 that χ_{CP} is reduced by a factor of 1.5, from around 0.526 ± 0.007 to 0.35 ± 0.02 (when $x_1 \approx 0.42$ – 0.44 , $v_{\text{ref}} = 0.1 \text{ nm}^3$). The deviation from the experimental χ_{CP} is reduced from more than 100% to around 35%, while the single-component properties of PEO-90 such as liquid densities, vapor pressures, and the critical point are still accurately reproduced. One

can calculate from Table S3 that the mean unsigned percentage error (MUPE) for three low-temperature liquid densities is 0.9% (original TraPPE-UA gives 0.6%), for unary vapor pressures is 7% (original TraPPE-UA gives 6%), and for the critical temperature is within 0.1% (original TraPPE-UA gives 0.7%).

Moreover, to show that modification of the alkane force field does not impact χ , we performed one set of simulations with scaled ϵ values for all the interaction sites in the alkane molecules ($\epsilon_{\text{CH}_3}/k_B = 100.9$ K and $\epsilon_{\text{CH}_2}/k_B = 47.4$ K). This set of ϵ reduces unary vapor pressures of *n*-dodecane to match the experimental ones, but note that this fix can lead to significant deviations in liquid densities and the critical temperature of unary alkanes. One can see from Figure 3 that despite much better agreement on the separation factor for the binary system (from cyan to orange in the top and middle panels), χ_{CP} remains approximately the same and shows little improvement. This finding suggests that χ only reflects the binary interactions between two unlike monomers regardless of the deviation in single-component vapor pressures. Since this crude modification of the alkane force field can result in inaccurate predictions of important thermodynamic properties such as liquid densities and the critical temperature, the modified TraPPE-UA ether force field was used to model PEO for the rest of this study (see Table 2) while the original TraPPE-UA force field was used to model alkanes.

RESULTS AND DISCUSSION

Molecular Weight Dependence of χ . Phase Diagram of PEP*-423/PEO Mixtures. Figure 4 shows simulated coexistence curves from LLE simulations and experimental cloud point curves for quasi-binary blends consisting of PEP*-423 and PEO with various M_n values ranging from 217 to 500 Da. Because of the relatively low dispersities of the PEO samples, the binary FH theory with $\chi(T)$ as the only adjustable parameter (eq 1) can be utilized to fit the binodal curves and extract $\chi_{\text{eff}}(T)$.^{31,62} Solid lines in Figure 4 are the fitted binodal curves obtained by using a molecular-weight-dependent but composition-independent functional form of $\chi_{\text{eff}}(T) = a(M)/T + b(M)$. The fitting results agree fairly well for both simulation coexistence curves and experimental cloud point curves. This suggests that the compositional dependence of χ can be neglected for PEP/PEO mixtures, which is consistent with earlier experimental studies on this system^{7,8} as well as the *n*-dodecane/PEO-178 simulation data shown in the previous section.

A comparison between simulation and experimental phase diagrams reveals that simulations overestimate the upper critical solution temperatures (UCSTs) by around 50 K. The overestimation in χ is the origin of this deviation. For example, the χ_{eff} values for $M_n = 500$ Da at $T = 450$ K are 0.29 and 0.39 for experimental and simulation data, respectively ($v_{\text{ref}} = 0.1 \text{ nm}^3$). This 35% overestimation (~ 0.1 in absolute magnitude) is in agreement with the 35% deviation (0.1 in absolute magnitude) in χ_{CP} for the *n*-dodecane/PEO-178 mixture. Despite the seemingly significant deviation, a 50 K overestimation in UCST corresponds to less than 1 kJ/mol in the free energy of transfer.⁵⁸ As a comparison, the original TraPPE-UA force field likely overestimates the UCST by more than 100 K. (At $T = 550$ K, the squalane weight fractions in the coexisting phases for the original force field are 88 ± 2 and 4 ± 1 wt %, while this temperature is already above the UCST of the modified force field used here.) Although the PEP/PEO interactions are still slightly too unfavorable even after the force field modification, the discrepancy between simulation and experimental results is sufficiently small that reliable results can be obtained regarding the effect of molecular weight and MWD on χ .

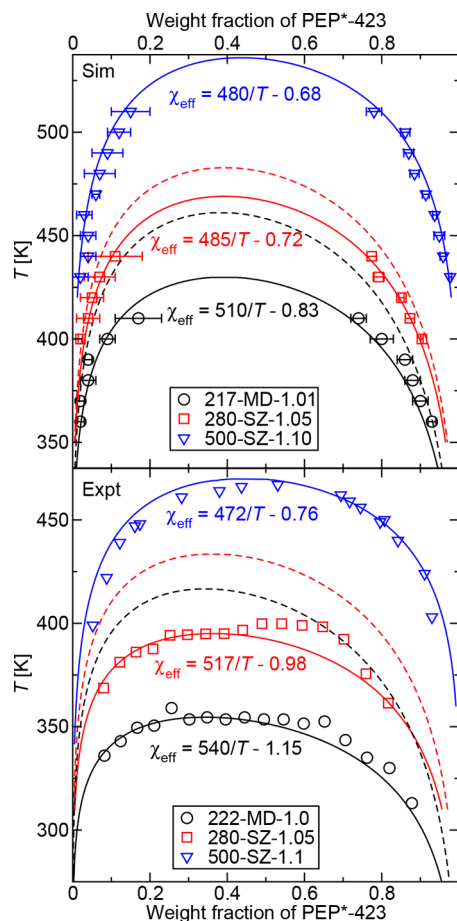


Figure 4. Simulated coexistence curves (top) and experimental cloud point curves (bottom) of PEP*-423/PEO mixtures. The experimental data for PEO-222-MD-1.0 and PEO-500-SZ-1.1 are from Xie and Lodge⁸ and Washburn et al.,⁶² respectively. Solid lines are the fitting results using eq 1 with $\chi_{\text{eff}}(M,T) = a(M)/T + b(M)$, in which a and b are fitting parameters. Dashed lines are calculated phase diagrams using eq 1 with molecular weight independent $\chi_{\text{eff}}(T)$ from the PEO-500 fit. Analytical expressions of the molecular-weight-dependent fits are provided, and the uncertainties of the fitting are estimated to be $\Delta\chi = \pm 0.01$, equivalent to UCST = ± 5 K.

For both simulation and experimental data, the fitted χ_{eff} increases with increasing PEO molecular weight. Furthermore, the theoretical phase diagrams for PEP*-423/PEO-222(PEO-217) and PEP*-423/PEO-280 mixtures were calculated using the $\chi_{\text{eff}}(T)$ deduced from PEP*-423/PEO-500-SZ-1.1 and are shown as dashed lines in Figure 4. One can see that if χ_{eff} is assumed to be molecular weight independent, the UCSTs of PEP*-423/PEO-222(PEO-217) and PEP*-423/PEO-280 mixtures are overestimated by about 60 and 30 K, respectively, for both simulation and experimental data sets. Therefore, one can conclude that χ of the PEP/PEO mixtures exhibits a non-negligible molecular weight dependence and that this dependence stands in contrast to the general trend in earlier literature (decreasing χ with increasing molecular weight^{10,21,24,77}).

VLE of Oligomeric PEP/PEO Mixtures. To further characterize and rationalize the molecular weight dependence of χ , we performed VLE simulations to compute χ_{CP} for oligomeric PEP/PEO mixtures ($\phi_{\text{PEP}} \approx 0.5$) with n ranging from two to six, and results are displayed in Figure 5. The densities of single-component oligomers, which are used to compute volume fractions of the mixtures, are provided in Table S9. These

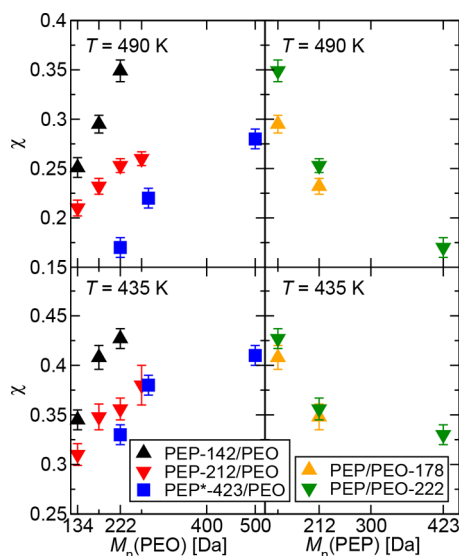


Figure 5. χ of oligomeric PEP/PEO mixtures as a function of the number-average molecular weight of PEP or PEO at $T = 435$ and 490 K. Data that contain PEP*-423 are χ_{eff} from LLE simulations (see Figure 4), while the remainder of the data are χ_{CP} from VLE simulations.

simulations reproduce the PEO molecular weight dependence of χ_{eff} from LLE simulations. For both PEP-142 and PEP-212, increasing the molecular weight of PEO results in an increase in χ_{CP} . In contrast, χ_{CP} decreases with the increasing molecular weight of PEP, which displays the molecular weight dependence found in other experimental studies.^{20,21} More importantly, molecular weight exerts a large impact on χ_{CP} at both temperatures investigated. For example, varying the PEP chain length can result in a difference in χ_{CP} by as much as a factor of 2 (or 0.2 in absolute magnitude) for the PEP/PEO-222 mixture at $T = 490$ K. This corresponds to a difference in the coexistence curve by about 100 K. Note that correlations used in the literature, such as $\chi_{\text{SANS}} \sim 1/N_{\text{AVE}}$ ^{21,22} are not applicable to this mixture (see Figure S12). Therefore, it is crucial to understand different molecular weight dependences for the two components and to develop an approach to predict χ for PEP/PEO pairs of arbitrary chain lengths.

The Hildebrand formalism states that χ is proportional to the solubility parameter differences between two components:

$$\begin{aligned} \chi_{\text{H}}(T) &= \frac{v_{\text{ref}}}{k_{\text{B}}T} [\delta_1(T) - \delta_2(T)]^2 \\ &= \frac{v_{\text{ref}}}{k_{\text{B}}T} [\sqrt{\Pi_{\text{CED},1}(T)} - \sqrt{\Pi_{\text{CED},2}(T)}]^2 \end{aligned} \quad (3)$$

where v_{ref} is the reference volume. The above equation can be used to qualitatively explain the molecular weight dependence of χ . Figure 6a shows the cohesive energy density Π_{CED} as a function of chain length that was used to compute χ from the Hildebrand formalism. One can see that $\Pi_{\text{CED}}(\text{PEO})$ are always higher than $\Pi_{\text{CED}}(\text{PEP})$ at both temperatures (e.g., $\Pi_{\text{CED}}(\text{PEO-222})$ is 1.7 times higher than that of $\Pi_{\text{CED}}(\text{PEP-212})$ at $T = 435$ K, despite the similar molecular weights). As the molecular weight of PEP increases, $[\delta(\text{PEP}) - \delta(\text{PEO})]^2$ shrinks, and thus, so does χ . On the other hand, when the molecular weight of PEO increases, $[\delta(\text{PEP}) - \delta(\text{PEO})]^2$ becomes larger, which leads to the increase in χ . This qualitative agreement suggests that the molecular weight dependence of δ is the origin of the

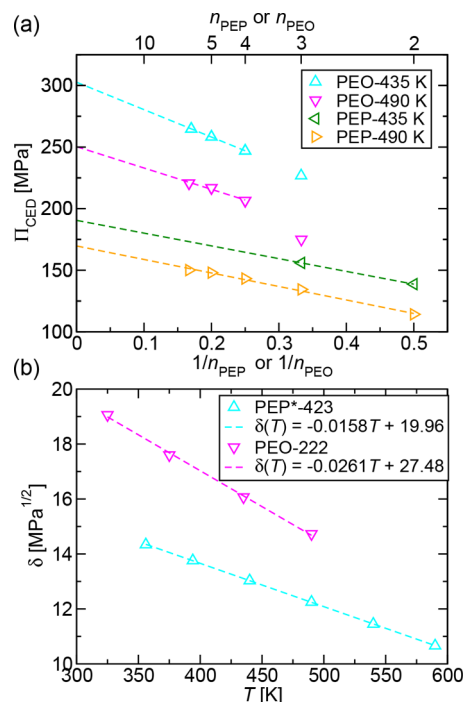


Figure 6. (a) Cohesive energy density, Π_{CED} , as a function of the inverse chain length of PEP and PEO. Dashed lines are linear fits to the data using data points with number of heavy atoms in PEP or PEO greater than or equal to 10 ($n_{\text{PEP}} \geq 2$ and $n_{\text{PEO}} \geq 4$). (b) Solubility parameter, δ , as a function of temperature for PEP*-423 and PEO-222. Dashed lines are linear fits of δ versus T .

molecular weight dependence of χ , which implies that for such polar/nonpolar polymeric mixtures the sign of the molecular weight dependence of χ is always opposite for the two components. For other mixtures such as polyolefins, this argument may not hold due to the relatively greater effect of other nonidealities on the mixing thermodynamics (e.g., finite compressibility, nonideal entropy of mixing).²⁵

To quantify the molecular weight dependence of δ , two linear relationships were utilized. First, Figure 6a reveals that Π_{CED} is linear with the inverse chain length when oligomers are sufficiently long (when the number of heavy atoms is greater than or equal to 10), which enables the estimation of $\Pi_{\text{CED}}(\text{PEP})$ and $\Pi_{\text{CED}}(\text{PEO})$ of arbitrary chain length at $T = 435$ and 490 K. Second, as shown in Figure 6b, δ is found to vary linearly with temperature for temperatures well below the vapor–liquid critical temperature. This further allows for the extrapolation of Π_{CED} and δ to other temperatures. Notably, the same linear relationships were also found in our earlier work for three olefin oligomers.¹⁸ The following equations were extracted from the two linear fits and can be used to obtain Π_{CED} and δ for PEP and PEO of arbitrary chain length and temperatures.

$$\begin{aligned} \Pi_{\text{CED}}(\text{PEP}, 435 \text{ K})/\text{MPa} &= -(103.6 \pm 0.3)/n \\ &+ (190.5 \pm 0.4) \quad (n \geq 2) \end{aligned} \quad (4)$$

$$\begin{aligned} \Pi_{\text{CED}}(\text{PEP}, 490 \text{ K})/\text{MPa} &= -(109.6 \pm 0.3)/n \\ &+ (169.7 \pm 0.5) \quad (n \geq 2) \end{aligned} \quad (5)$$

$$\begin{aligned} \Pi_{\text{CED}}(\text{PEO}, 435 \text{ K})/\text{MPa} &= -(222.7 \pm 0.2)/n \\ &+ (302.7 \pm 0.3) \quad (n \geq 4) \end{aligned} \quad (6)$$

$$\begin{aligned} \Pi_{\text{CED}}(\text{PEO}, 490 \text{ K})/\text{MPa} &= -(173.4 \pm 0.3)/n \\ &+ (250.3 \pm 0.4) \quad (n \geq 4) \end{aligned} \quad (7)$$

$$\begin{aligned} \delta(n_{\text{PEP}}, n_{\text{PEO}}, T)/\text{MPa}^{1/2} &= [\sqrt{\Pi_{\text{CED}}(490 \text{ K})} \\ &- \sqrt{\Pi_{\text{CED}}(435 \text{ K})}] \frac{T - 435}{55} + \sqrt{\Pi_{\text{CED}}(435 \text{ K})} \end{aligned} \quad (8)$$

A more quantitative model is constructed by using the following equation,^{78,79} in which k_{ij} is the only adjustable parameter that quantifies the deviation from the Berthelot combining rule used in the Hildebrand formalism:

$$\begin{aligned} \chi_{\text{SP}}(T) &= \frac{v_{\text{ref}}}{k_{\text{B}}T} [\Pi_{\text{CED},1}(T) + \Pi_{\text{CED},2}(T) \\ &- 2k_{ij}\sqrt{\Pi_{\text{CED},1}(T)\Pi_{\text{CED},2}(T)}] \end{aligned} \quad (9)$$

When k_{ij} is unity, eq 3 is recovered. For PEP/PEO mixtures, one can use eqs 4–9 and obtain an explicit nonlinear expression of $\chi(n_{\text{PEP}}, n_{\text{PEO}}, T)$ (see eq 1 in the Supporting Information). For simulations, empirical fitting to the χ_{CP} values yields a k_{ij} value of 0.975 ± 0.003 . The utility of this k_{ij} value is confirmed by using χ_{eff} from LLE simulations as the validation set. Figure 7 reveals that the calculated χ_{SP} using this

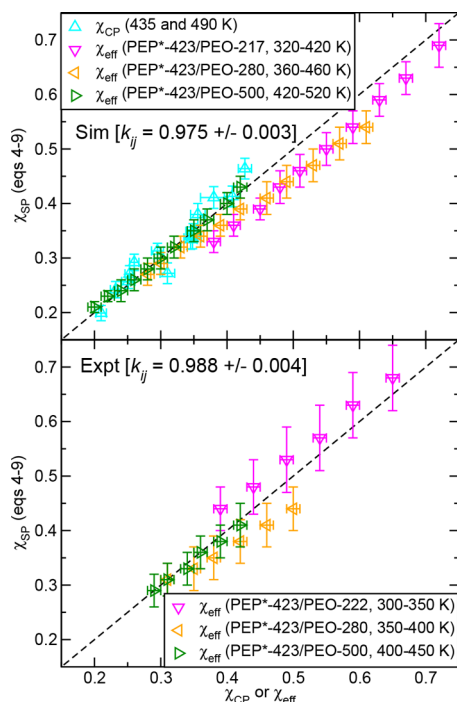


Figure 7. χ_{SP} as a function of χ_{CP} or χ_{eff} for PEP/PEO mixtures. k_{ij} values are fitted using χ_{CP} (cyan) and all data points for simulation and experiments, respectively.

k_{ij} value agrees with χ_{CP} and χ_{eff} with MUPE for all the data points being $6 \pm 4\%$ (6% is roughly 0.02 in absolute magnitude) and the maximum absolute error being 0.06 ± 0.03 . The average error approaches the average uncertainty of the simulation data. It corresponds to a deviation in the mixture UCST of about 10 K, while the maximum error corresponds to

a deviation of about 25 K. As for experiments, due to the lack of χ for shorter PEP/PEO mixtures, all the χ_{eff} data are used for the fitting, which results in a k_{ij} value of 0.988 ± 0.004 . The MUPE for all the experimental data points are $6 \pm 4\%$, and the maximum absolute error is 0.06 ± 0.04 . The discrepancy in simulated and experimental k_{ij} values reflects the inaccuracy of the PEP–PEO interactions in the nonpolarizable molecular model. If the force field were sufficiently accurate, $k_{ij}(\text{sim})$ and $k_{ij}(\text{expt})$ should converge, which implies that simulations can accurately predict $\chi(M, T)$.

To demonstrate that χ_{SP} computed from eq 9 can be used to calculate coexistence curves, predicted coexistence curves using the fitted k_{ij} values as well as a k_{ij} value of unity are shown in Figure 8. One can see that the maximum error between

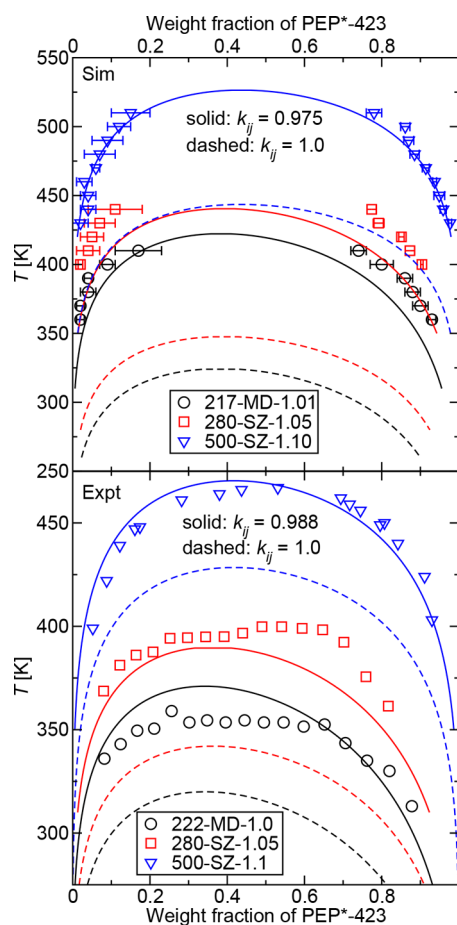


Figure 8. Predicted coexistence curves for PEP*-423/PEO mixtures for simulation (top) and experiments (bottom). The symbols are simulation and experimental data. Solid lines are from eq 9 using k_{ij} values of 0.975 and 0.988 for simulation and experiments, respectively. Dashed lines are from eq 9 using a k_{ij} value of 1.0.

simulations/experiments and eq 9 predictions using $k_{ij}(\text{sim}) = 0.975/k_{ij}(\text{expt}) = 0.988$ is less than 20 K. When a k_{ij} value of 1.0 is used, the predicted coexistence curves deviate significantly from the simulation or experimental data, with the average error greater than 100 K. This result suggests that it is essential to fit a k_{ij} value from existing simulation or experimental data in order to predict χ and coexistence curves of binary polymer blends with arbitrary molecular weights.

The data in Figure 8 show large deviations for the mixtures with the two shorter PEO chains that exhibit miscibility gaps

shifted to lower temperatures. This may be an indication of a weak temperature dependence for k_{ij} , which is consistent with recent calculations of water/oil interfacial tension.⁷⁸ The explanation for why k_{ij} for this system is smaller than unity is that PEO–PEO interactions include first-order electrostatic contributions that are not present for the PEP–PEP and PEP–PEO interactions (lumping first- and second-order electrostatic interactions). Therefore, PEP–PEO interactions predicted from eq 3 are too favorable, and thus, a k_{ij} value that is smaller than one is essential to correct the underestimation in χ . Similarly, $k_{ij}(\text{sim})$ is smaller than $k_{ij}(\text{expt})$ because the dipole-induced dipole interactions that are present in real systems are missing in the nonpolarizable TraPPE-UA model, leading to the overestimation in χ for the simulated systems. Furthermore, the origin of the temperature dependence of k_{ij} is the temperature-dependent contribution from first-order dipole–dipole interactions due to the Boltzmann averaging of orientation.⁷³ However, despite the success in the qualitative agreement mentioned above, we know from the binodal curve fitting that an entropic deviation from the FH theory is also lumped into χ_{eff} . Future studies on other molecular systems with wider temperature ranges and calculation/measurement of the heat of mixing are needed to elucidate the physical meaning of k_{ij} .

Effects of MWD and \mathcal{D} on the Phase Diagram. LLE of PEP*-423/PEO-500 Mixtures. Figure 9 displays liquid–liquid coexistence curves from simulations and experimental cloud point curves for quasi-binary mixtures consisting of near-monodisperse PEP*-423 ($\mathcal{D} = 1.04$) and polydisperse PEO with $M_n \approx 500$ Da, but with various MWDs and \mathcal{D} values. Simulated coexistence curves corresponding to PEO-500-SZ-1.02, PEO-500-SZ-1.10, PEO-500-SZ-1.19, and PEO-500-BM-1.12 (\mathcal{D} varying from 1.02 to 1.19) are indistinguishable from each other within statistical uncertainties. This is confirmed by the near identical experimental cloud point curves for PEO-500-SZ-1.1 and PEO-500-BM-1.1. These results reveal that regardless of MWD, \mathcal{D} exerts a negligible influence on the phase diagram when \mathcal{D} is smaller than 1.2. Similar conclusions have also been reached by other experimental studies for high molecular weight polymers in solution.²⁷

However, coexistence curves of PEP*-423/PEO-500-BM-1.76, in which the PEO has the “extreme” bimodal distribution containing 57 mol % (15 wt %) of PEO-134 and 43 mol % (85 wt %) of PEO-1015 ($\mathcal{D} = 1.76$), show significant deviation from those with smaller dispersities. The binary representation of the phase diagram is shown in Figure 9a, and the ternary phase composition data are provided in Figure 9b and Table S6. Despite the increased complexity of the ternary phase diagram, the two major assumptions in the simulations are still valid. First, the liquid–liquid equilibria setup is appropriate because the molecular weight ratio between the two PEO components $r = M(\text{PEO-1015})/M(\text{PEO-134})$ is 7.6, which is lower than the three-phase separation limit of $r^* = 13$ from the generalized FH theory.⁸⁰ Furthermore, we cannot transfer PEO-1015 to the alkane phase due to the lack of medium molecular weight PEO molecules as transfer intermediates. Nevertheless, the assumption that PEO-1015 always stays in the PEO-rich phase is supported by the negligible solubility of PEO-1015 in PEP*-423 (less than 1 wt % at $T = 500$ K), estimated from eq 1 with a χ_{SP} value from eqs 4–9.

Two features in the coexistence curve of the PEP*-423/PEO-500-BM-1.76 mixture stand in contrast to those containing low-dispersity PEO. First, the quasi-binary compo-

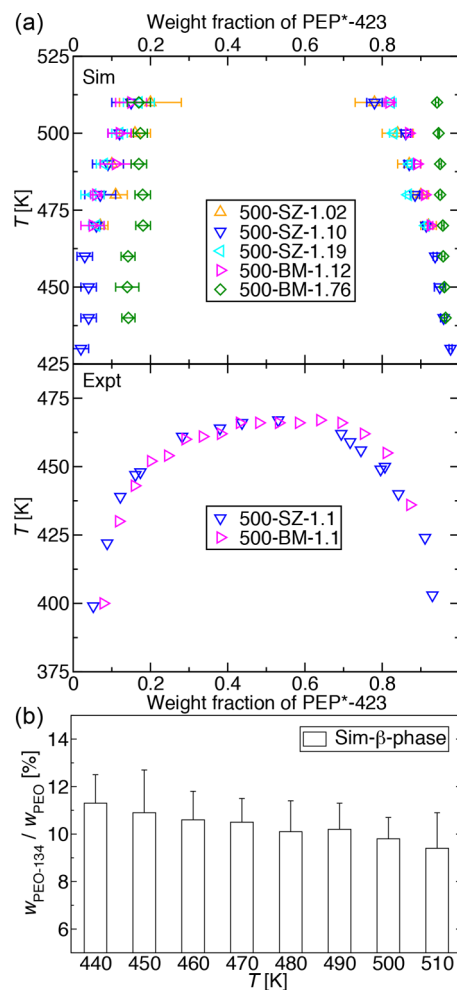


Figure 9. (a) Simulated coexistence curves (top) and experimental cloud point curves (bottom) for PEP*-423/PEO-500 mixtures. Experimental data for PEO-500-SZ-1.1 are from Washburn et al.⁶² (b) Weight fraction of PEO-134 among all PEO molecules in the PEO-rich phase for the PEP*-423/PEO-500-BM-1.76 mixture.

sitions are relatively insensitive to the temperature, with the solubility of PEP*-423 in the PEO-rich phase changing from 14.3 ± 1.7 wt % at $T = 440$ K to merely 17 ± 3 wt % at $T = 510$ K. This can also be deduced from the weight fraction of PEO-134 among all the PEO molecules in the PEO-rich phase (this fraction is unity in the PEP-rich phase), shown in Figure 9b. The decrease of PEO-134 weight fraction as a function of temperature is on the order of the simulation uncertainties. The temperature insensitivity can mainly be attributed to the dominant overall weight fraction of PEO-1015 among all the PEO molecules (85 wt %). Consequently, the distribution change of PEO-134 hardly influences the coexistence curve. For example, when the temperature increases from 440 to 510 K, the mole fraction of PEO-134 in the PEP-rich phase increases by around 50% (from 10.1 ± 0.9 to 15.1 ± 1.0 mol % or from 3.6 ± 0.3 to 5.8 ± 0.4 wt % on the weight fraction scale). The second feature of interest is that the PEP solubility in the PEO-rich phase is much higher at low temperatures ($T \leq 500$ K) compared to that of PEO-500-BM-1.12. For example, at $T = 470$ K, the PEP solubility in PEO-500-BM-1.76 (18.1 ± 1.9 wt %) is about a factor of 3–4 higher than that of PEO-500-BM-1.12 (5 ± 3 wt %). The increase in solubility can be explained by the more favorable interactions between PEP and PEO,

which will be more quantitatively elaborated later when the PEP free energy of transfer data are discussed. This deviation from other data sets clearly shows the failure of treating this ternary mixture as a binary one. Unfortunately, the theoretical treatment of the ternary mixture can be much more complicated since the binary interaction parameter χ is a function of composition when the third component is the majority species in weight or volume fraction.⁸¹ In summary, this result reveals that for mixtures with a bimodal distribution and a large dispersity, which can be the case for many industrial polymers, the treatment of the mixture as a quasi-binary blend can introduce non-negligible errors.

The effect of dispersity on molecular partitioning raises the question of why the overall phase diagram is not significantly perturbed by changing from SZ-1.02 to SZ-1.19. Mixtures containing PEO with larger dispersity (e.g., PEO-500-SZ-1.76) would be of interest but are more challenging for simulation because of the need for a larger number of components to represent the SZ versus the BM distribution. The molecular weight dependence of the free energy of transfer ΔG_{trans} can be used to address this question, which is calculated from the following equation:^{66,73,82}

$$\Delta G_{\text{trans}}(\beta \rightarrow \alpha) = -k_{\text{B}}T \ln(\rho_{\alpha}/\rho_{\beta}) \quad (10)$$

where ρ_i is the number density of PEP or PEO in phase i . Note that ρ_i can be obtained from either simulations or experiments using the composition and the density of phase i . Figure 10

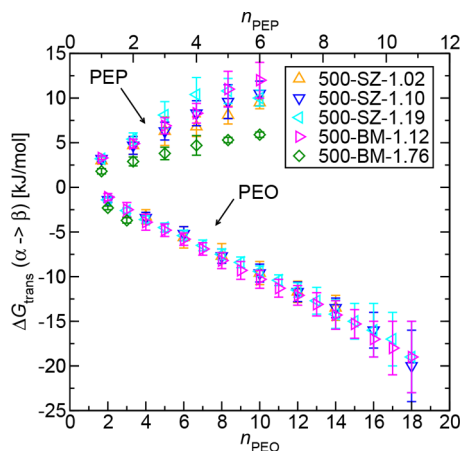


Figure 10. Free energy of transfer (ΔG_{trans}) from the PEP-rich (α) to the PEO-rich phase (β) as a function of the PEP and PEO chain lengths at $T = 470$ K.

depicts ΔG_{trans} from the PEP-rich (α) to the PEO-rich (β) phase as a function of the chain length for both PEP and PEO at $T = 470$ K. ΔG_{trans} is found to be a linear function of chain length for both types of molecule, and the values do not change with respect to the MWD or \mathcal{D} , with the exception of PEO-500-BM-1.76. For the mixtures with $\mathcal{D} < 1.2$, the incremental transfer free energies are found to be 2.0 ± 0.4 and 1.0 ± 0.1 kJ/mol for one PEP and PEO repeat unit, respectively.

We can obtain the effect of dispersity on compositions and MWDs for both phases using continuous thermodynamics.^{31–33} For the partitioning of PEO between two phases, we have the following:

$$K_{\alpha} = \frac{\rho_{\alpha}}{\rho_{\beta}} = \exp\left[\frac{-\Delta G_{\text{trans}}(\beta \rightarrow \alpha)}{k_{\text{B}}T}\right] = \exp\left[\frac{-k_{\text{trans}}(\beta \rightarrow \alpha)M_{\text{PEO}}}{k_{\text{B}}T}\right] \quad (11)$$

in which K_{α} is the partition constant and $\Delta G_{\text{trans}}(\beta \rightarrow \alpha) = k_{\text{trans}}(\beta \rightarrow \alpha)M_{\text{PEO}}$. This equation shows that K_{α} increases or decreases exponentially as the chain length increases. The total mass of PEO partitioned in both phases m_{α}^{PEO} and m_{β}^{PEO} can be expressed by the following two equations:

$$m_{\alpha}^{\text{PEO}} = \int_0^{\infty} P_{\alpha}(M) dM = \int_0^{\infty} P(M) \frac{K_{\alpha}(M)K_v}{K_{\alpha}(M)K_v + 1} dM \quad (12)$$

$$m_{\beta}^{\text{PEO}} = \int_0^{\infty} P_{\beta}(M) dM = \int_0^{\infty} P(M) \frac{1}{K_{\alpha}(M)K_v + 1} dM \quad (13)$$

in which $P(M)$ is the total MWD in mole fraction, $P_i(M)$ is the MWD in phase i , and K_v is the volume ratio between the two phases, and it can be calculated via

$$K_v = \frac{V_{\alpha}}{V_{\beta}} = \frac{m_{\alpha}/\rho_{\alpha}}{m_{\beta}/\rho_{\beta}} = \frac{\rho_{\beta}(w_{\beta} - w_{\text{tot}})}{\rho_{\alpha}(w_{\text{tot}} - w_{\alpha})} \quad (14)$$

where V_i , m_i , ρ_i , and w_i are the volume, mass, density, and PEO weight fraction of phase i , respectively; w_{tot} is the total weight fraction of PEO. If we assume that the partitioning of PEP*-423 is not affected by the dispersity of PEO (free energy of transfer of PEP is not a function of dispersity from Figure 10), we can solve eqs 11–14 together with the mass balance to compute w_i and K_v given the total weight fraction w_{tot} and the original MWD $P(M)$. The solution can provide the effect of dispersity on the coexistence curve and quantify the MWD in each phase.

Figure 11 shows the calculated PEO compositions in both phases as a function of dispersity for the PEP*-423/PEO-500 mixture when PEO has a Schulz–Zimm overall distribution. The $k_{\text{trans}}(\beta \rightarrow \alpha)$ value of 22.5 ± 2.5 J/g from Figure 10 is used. One can see that the calculated compositions agree fairly well with the simulated ones within uncertainties, which serves as a self-consistency check. In addition, the lines are almost flat,

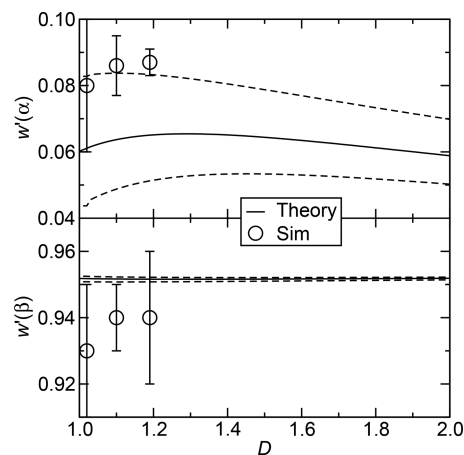


Figure 11. Weight fraction of PEO in α (top) and β (bottom) phase as a function of dispersity for the PEP*-423/PEO-500 mixture when PEO has the Schulz–Zimm overall distribution at $T = 470$ K. Symbols are simulation data, while solid and dashed lines are the calculated values and uncertainties from eqs 11–14 and Figure 10, respectively.

which suggests that dispersity does not exert a large influence on the coexisting compositions for the SZ distribution at $T = 470$ K for $\bar{D} \leq 2$. The result is consistent with the simulation and experimental findings for PEP*-423/PEO-500-SZ mixtures. The comparison between the predicted coexistence curve for PEP*-423/PEO-500-SZ-1.76 and the simulated coexistence curve for PEP*-423/PEO-500-BM-1.76 suggests that the shape of the MWD plays a pivotal role in the effect of dispersity on the polymer mixture phase diagram (e.g., the effect of dispersity is more obvious for the BM MWD). For other overall MWDs and molecular weights, one can use the numerical method formulated here to obtain an estimate regarding the effect of dispersity.

Theoretical calculation reveals that the change in free energy of transfer is the key to the shift in composition for the PEP*-423/PEO-500-BM-1.76 mixture. From Figure 10, one can see that the free energy of transfer of PEP in the PEP*-423/PEO-500-BM-1.76 mixture at $T = 470$ K deviates substantially from the rest of the data set. The smaller free energy barrier for PEP to transfer to the PEO-rich phase is the origin of the higher PEP concentration in the PEO-rich phase. Similarly, the slightly higher free energy barrier for low molecular weight PEO to transfer into the PEP-rich phase coincides with the lower PEO-134 composition in the PEP-rich phase at equilibrium for the PEP*-423/PEO-500-BM-1.76 mixture. The shift in transfer free energy implies that the quasi-binary approximation fails when the dispersity of PEO is as large as 1.76. It also suggests that the binary interaction parameter χ is a function of the composition in the ternary mixture. For example, when the composition of the PEO-rich phase changes from PEO-500-SZ-1.19 to PEO-500-BM-1.76 (the compositions of the PEP-rich phase are similar), it becomes more favorable for PEO-134 to transfer into the PEO-rich phase, with ΔG_{trans} changing from -2.6 ± 0.3 to -3.7 ± 0.3 kJ/mol, due likely to the presence of high-molecular-weight PEO molecules.

Molecular Partitioning. The partitioning of different molecular weight PEO molecules is revealed by the MWD in each phase from LLE simulations (symbols) and theoretical calculations (lines) as shown in Figure 12. The agreement between simulation data and theoretical calculations demonstrates the robustness of the numerical formulation eqs 11–14. When the dispersity is low ($\bar{D} = 1.02$), the MWDs for both phases are almost identical. When the dispersity increases to $\bar{D} = 1.10$, a distinction between the two distributions emerges at the higher molecular weight end of the distribution. For example, the mole fraction of PEO-707 among all the PEO molecules in the PEO-rich phase is 80% higher than that in the PEP-rich phase. This indicates an enrichment of higher molecular weight PEO molecules in the PEO-rich phase, which is consistent with the lower solubility of higher molecular weight PEO in the PEP-rich phase. When \bar{D} further increases to 1.19, the distinction between two MWDs becomes more pronounced.

This effect of MWD can also be quantified by the $M_n(\text{PEO})$ present in each phase shown in Figure 12b. It is apparent that for both types of MWD $M_n(\text{PEO})$ is higher in the PEO-rich phase, and the gap between the two M_n values in each phase grows, as the overall dispersity increases. When $\bar{D} = 1.19$, $M_n(\text{PEO})$ in the PEO-rich phase is 50% higher than that in the PEP-rich phase at $T = 470$ K. For the bimodal distribution, $M_n(\text{PEO})$ in both phases are lower than those of the Schulz–Zimm distribution when \bar{D} values are close. This is due to the higher abundance of lower molecular weight PEO in the overall

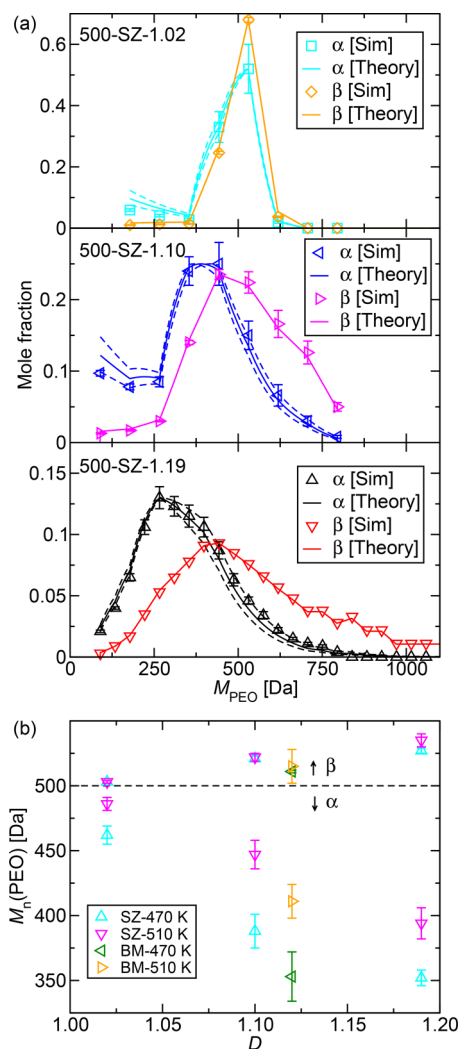


Figure 12. (a) PEO MWD in the PEP-rich (α) and the PEO-rich (β) phases at $T = 470$ K for PEP*-423/PEO mixtures with various dispersities. Symbols represent simulation data, while solid and dashed lines represent theoretical calculations and the uncertainties using eqs 11–14, respectively. (b) $M_n(\text{PEO})$ as a function of dispersity.

MWD as well as fewer high molecular weight molecules in the Schulz–Zimm distribution. The difference in partitioning is the thermodynamic driving force of fractionation of disperse polymers.^{40,83} Moreover, Figure 12 also reveals that the MWDs of polymers in each phase can differ even if the overall compositions in the phase diagram are similar. For example, when $T = 470$ K, $M_n(\text{PEO})$ in the PEP-rich phase can vary from 462 ± 7 to 352 ± 6 Da when \bar{D} increases from 1.02 to 1.19, but the corresponding phase diagrams are nearly identical (see Figure 9). Therefore, the approximation that such a quasi-binary mixture can be treated as a two-component system can be misleading, and caution needs to be taken if the exact content of the polymer in each phase is of interest.

Structural Analysis. The effect of liquid structure on the mixing thermodynamics is characterized by the intermolecular radial distribution functions (RDFs) computed from the simulation trajectories, plotted in Figure 13. For both PEP*-423/PEO-500-SZ-1.10 and PEP*-423/PEO-217-MD-1.01 mixtures at a relatively high temperature near their UCSTs, the peak positions of the oxygen–oxygen RDF for intermolecular PEO–PEO pairs in both phases (solid and dashed lines in red)

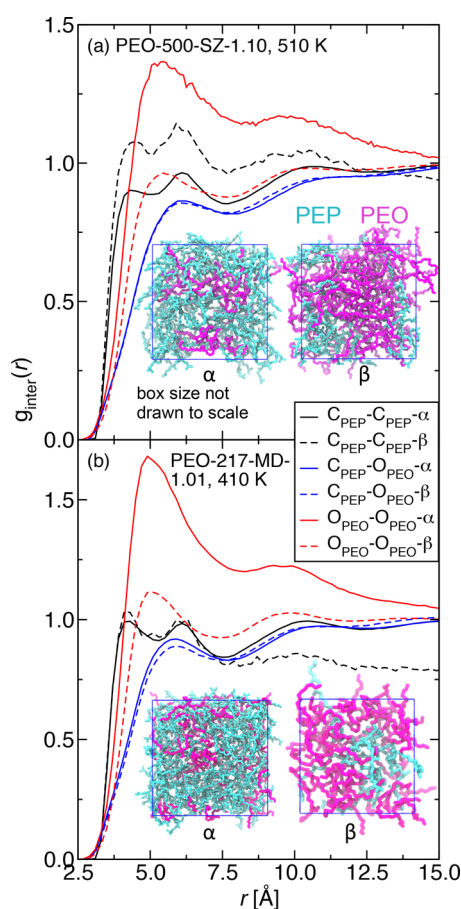


Figure 13. Intermolecular radial distribution functions $g_{\text{inter}}(r)$ and representative simulation snapshots for the two PEP*/-423/PEO mixtures. The number integral is provided in Figure S11.

are similar. Nevertheless, the height of the RDFs is vastly dwarfed in the PEO-rich phase compared to that corresponding to the PEP-rich phase. This is an indication of the clustering behavior of PEO molecules in the minority phase. Similar aggregation behavior can also be seen for PEP–PEP pairs in the PEO-rich phase containing PEO-500-SZ-1.10 (dashed black lines in the top panel), but the distinction between two carbon–carbon RDFs for the mixture with shorter PEO chains PEO-217-MD-1.01 is less obvious (solid and dashed lines in black in the bottom panel). In contrast, the carbon–oxygen RDFs for the PEP–PEO pair in two phases (solid and dashed lines in blue) are found to trace closely to each other, revealing no sign of PEP–PEO aggregation. The clustering behavior agrees with our finding that the entropic contribution to χ is always a significant portion of the total χ (i.e., the intercept b in the $\chi = a/T + b$ fitting is nonzero). In addition, the aggregation behavior is consistent with other simulations of polymer blends^{84,85} and block polymers.^{17,86–88} The simulation snapshots depicted in Figure 13 also confirm the clustering behavior. Both PEP and PEO molecules tend to aggregate when they are the minority components. This clustering behavior reflects the incompatibility of the two components and further reveals the complexity of mixing behavior that deviates significantly from the ideal mixing assumption of the FH theory.

CONCLUSIONS

This work utilizes GEMC simulation in conjunction with experimental cloud point measurements to study the phase behavior of oligomeric PEP/PEO mixtures. The utilization of a modified TraPPE–UA force field for PEO greatly improves the accuracy of the computed χ_{CP} for alkane/ether mixtures, but it still results in an overestimation of χ_{CP} by around 35% (or 0.1 in absolute magnitude) and, thus, overestimation of the coexistence curves for binary alkane/ether mixtures. Results from simulations and experiments combined shed light on the molecular weight dependence of χ and the effect of MWD and \mathcal{D} on the liquid–liquid phase diagram. First, χ_{eff} or χ_{CP} of PEP/PEO mixtures increases as the molecular weight of PEO increases or as the PEP molecular weight decreases. This seemingly irregular dependence is rationalized by the chain length dependence of the cohesive energy densities for PEP and PEO. A modified Berthelot mixing rule with a single adjustable parameter k_{ij} has been established to rationalize the dependence and accurately predict χ for PEP/PEO mixtures of arbitrary molecular weights. For simulation data, k_{ij} is fitted to χ_{CP} of shorter oligomer mixtures and yields a value of 0.975 ± 0.003 . This value differs from the k_{ij} fitted to the experimental cloud point curves of PEP*/-423/PEO mixtures (0.988 ± 0.004) due to the inaccuracy of the force field. For both simulation and experiments, the predicted coexistence curves using these k_{ij} values agree with those for PEP*/-423/PEO mixtures with less than 20 K error, while the deviation is more than 100 K if k_{ij} is unity (the Hildebrand formalism). Second, the binodal curves of PEP*/-423/PEO-500 mixtures with varying MWD and \mathcal{D} of PEO are investigated. Experiments and simulations both indicate no significant change in the coexisting phase compositions when the dispersity is below 1.2. However, the phase diagram shifts dramatically when a bimodal distribution is used ($\mathcal{D} = 1.76$). The shift suggests that the quasi-binary approximation fails when one component has a bimodal distribution with a large \mathcal{D} , and the ternary treatment is essential to describe the phase behavior of the mixture. The molecular partitioning extracted from simulations reveals the enrichment of high-molecular-weight PEO in the PEO-rich phase, which causes a decrease of $M_n(\text{PEO})$ in the PEP-rich phase as \mathcal{D} increases. This suggests that PEO compositions can be quite different even if the phase diagrams in weight fraction units are similar. Furthermore, structural analysis from simulations shows signs of aggregation for PEP and PEO molecules in their minority phases, which leads to deviations from the ideal mixing behavior and brings more complexity to the prediction of its phase behavior.

ASSOCIATED CONTENT

Supporting Information

The Supporting Information is available free of charge on the ACS Publications website at DOI: 10.1021/acs.macromol.8b00604.

Experimental characterization of PEO samples, additional simulation data for modification of molecular models, and numerical data presented in the main text (PDF)

AUTHOR INFORMATION

Corresponding Authors

*E-mail: lodge@umn.edu (T.P.L.).

*E-mail: siepmann@umn.edu (J.I.S.).

ORCID 

Qile P. Chen: 0000-0003-2697-8763

Shuyi Xie: 0000-0001-7966-1239

Timothy P. Lodge: 0000-0001-5916-8834

J. Ilja Siepmann: 0000-0003-2534-4507

Author Contributions

Q.P.C. and S.X. contributed equally to this work.

Notes

The authors declare no competing financial interest.

ACKNOWLEDGMENTS

This work was supported primarily by the National Science Foundation through the University of Minnesota MRSEC under Award DMR-1420013. Computer resources were provided through this NSF award and also by the Minnesota Supercomputing Institute at the University of Minnesota. Partial support (S.X.) was also received from the Office of Basic Energy Sciences (BES) of the U.S. Department of Energy (DOE), under contract No. DE-FOA-0001664.

REFERENCES

- (1) Jeon, H. S.; Lee, J. H.; Balsara, N. P. Predictions of the Thermodynamic Properties of Multicomponent Polyolefin Blends from Measurements on Two-component Systems. *Macromolecules* **1998**, *31*, 3328–3339.
- (2) Xu, J.; Mittal, V.; Bates, F. S. Toughened Isotactic Polypropylene: Phase Behavior and Mechanical Properties of Blends with Strategically Designed Random Copolymer Modifiers. *Macromolecules* **2016**, *49*, 6497–6506.
- (3) Bai, L.; He, S.; Fruehwirth, J. W.; Stein, A.; Macosko, C. W.; Cheng, X. Localizing Graphene at the Interface of Cocontinuous Polymer Blends: Morphology, Rheology, and Conductivity of Cocontinuous Conductive Polymer Composites. *J. Rheol.* **2017**, *61*, 575–587.
- (4) Li, T.; Heinzer, M. J.; Francis, L. F.; Bates, F. S. Engineering Superior Toughness in Commercially Viable Block Copolymer Modified Epoxy Resin. *J. Polym. Sci., Part B: Polym. Phys.* **2016**, *54*, 189–204.
- (5) Flory, P. J. Thermodynamics of High Polymer Solutions. *J. Chem. Phys.* **1942**, *10*, 51–61.
- (6) Huggins, M. L. Solutions of Long Chain Compounds. *J. Chem. Phys.* **1941**, *9*, 440–440.
- (7) Irwin, M. T.; Hickey, R. J.; Xie, S.; Bates, F. S.; Lodge, T. P. Lithium Salt-Induced Microstructure and Ordering in Diblock Copolymer/Homopolymer Blends. *Macromolecules* **2016**, *49*, 4839–4849.
- (8) Xie, S.; Lodge, T. P. Phase Behavior of Binary Polymer Blends Doped with Salt. *Macromolecules* **2018**, *51*, 266–274.
- (9) Balsara, N. P.; Fetters, L. J.; Hadjichristidis, N.; Lohse, D. J.; Han, C. C.; Graessley, W. W.; Krishnamoorti, R. Thermodynamic Interactions in Model Polyolefin Blends Obtained by Small-Angle Neutron Scattering. *Macromolecules* **1992**, *25*, 6137–6147.
- (10) De Gennes, P. *Scaling Concepts in Polymer Physics*; Cornell University Press: Ithaca, NY, 1979.
- (11) Schweizer, K. S. Analytic PRISM Theory of Structurally Asymmetric Polymer Blends and Copolymers. *Macromolecules* **1993**, *26*, 6050–6067.
- (12) Freed, K. F.; Dudowicz, J. Influence of Short Chain Branching on the Miscibility of Binary Polymer Blends: Application to Polyolefin Mixtures. *Macromolecules* **1996**, *29*, 625–636.
- (13) White, R. P.; Lipson, J. E. G. Free Volume, Cohesive Energy Density, and Internal Pressure as Predictors of Polymer Miscibility. *Macromolecules* **2014**, *47*, 3959–3968.
- (14) Heine, D.; Wu, D. T.; Curro, J. G.; Grest, G. S. Role of Intramolecular Energy on Polyolefin Miscibility: Isotactic Polypropylene/polyethylene Blends. *J. Chem. Phys.* **2003**, *118*, 914–924.
- (15) Jaramillo, E.; Wu, D. T.; Grest, G. S.; Curro, J. G. Anomalous Mixing Behavior of Polyisobutylene/polypropylene Blends: Molecular Dynamics Simulation Study. *J. Chem. Phys.* **2004**, *120*, 8883–8886.
- (16) Groot, R. D.; Warren, P. B. Dissipative Particle Dynamics: Bridging the Gap between Atomistic and Mesoscopic Simulation. *J. Chem. Phys.* **1997**, *107*, 4423–4435.
- (17) Chremos, A.; Nikoubashman, A.; Panagiotopoulos, A. Z. Flory-Huggins Parameter χ , from Binary Mixtures of Lennard-Jones Particles to Block Copolymer Melts. *J. Chem. Phys.* **2014**, *140*, 054909.
- (18) Chen, Q. P.; Chu, J. D.; DeJaco, R. F.; Lodge, T. P.; Siepmann, J. I. Molecular Simulation of Olefin Oligomer Blend Phase Behavior. *Macromolecules* **2016**, *49*, 3975–3985.
- (19) Zhang, W.; Gomez, E. D.; Milner, S. T. Predicting Flory-Huggins χ from Simulations. *Phys. Rev. Lett.* **2017**, *119*, 017801.
- (20) Han, C. C.; Bauer, B. J.; Clark, J. C.; Muroga, Y.; Matsushita, Y.; Okada, M.; Tran-cong, Q.; Chang, T.; Sanchez, I. C. Temperature, Composition and Molecular-Weight Dependence of the Binary Interaction Parameter of Polystyrene/poly (vinyl methyl ether) Blends. *Polymer* **1988**, *29*, 2002–2014.
- (21) Nedoma, A. J.; Robertson, M. L.; Wanakule, N. S.; Balsara, N. P. Measurements of the Composition and Molecular Weight Dependence of the Flory-Huggins Interaction Parameter. *Macromolecules* **2008**, *41*, 5773–5779.
- (22) Nedoma, A. J.; Robertson, M. L.; Wanakule, N. S.; Balsara, N. P. Measurements of the Flory-Huggins Interaction Parameter Using a Series of Critical Binary Blends. *Ind. Eng. Chem. Res.* **2008**, *47*, 3551–3553.
- (23) Teran, A. A.; Balsara, N. P. Thermodynamics of Block Copolymers with and without Salt. *J. Phys. Chem. B* **2014**, *118*, 4–17.
- (24) Morse, D. C.; Chung, J. K. On the Chain Length Dependence of Local Correlations in Polymer Melts and a Perturbation Theory of Symmetric Polymer Blends. *J. Chem. Phys.* **2009**, *130*, 224901.
- (25) Knychala, P.; Timachova, K.; Banaszak, M.; Balsara, N. P. 50th Anniversary Perspective: Phase Behavior of Polymer Solutions and Blends. *Macromolecules* **2017**, *50*, 3051–3065.
- (26) Kita, R.; Kubota, K.; Dobashi, T. Static and Dynamic Light Scattering of a Critical Polydisperse Polymer Solution. *Phys. Rev. E: Stat. Phys., Plasmas, Fluids, Relat. Interdiscip. Top.* **1998**, *58*, 793.
- (27) Kita, R.; Dobashi, T.; Yamamoto, T.; Nakata, M.; Kamide, K. Coexistence Curve of a Polydisperse Polymer Solution near the Critical Point. *Phys. Rev. E: Stat. Phys., Plasmas, Fluids, Relat. Interdiscip. Top.* **1997**, *55*, 3159.
- (28) Nakata, M.; Dobashi, T. Coexistence Curve of Polystyrene in Methylcyclohexane. V. Critical Behavior of the Three-Phase Coexistence Curve. *J. Chem. Phys.* **1986**, *84*, 5782–5786.
- (29) Nakata, M.; Dobashi, T.; Inakuma, Y.; Yamamura, K. Coexistence Curve of Polystyrene in Methylcyclohexane. X. Two-Phase Coexistence Curves for Ternary Solutions Near the Tricritical Compositions. *J. Chem. Phys.* **1999**, *111*, 6617–6624.
- (30) Shen, W.; Smith, G. R.; Knobler, C. M.; Scott, R. L. Tricritical Phenomena in Bimodal Polymer Solutions: Three-Phase Coexistence Curves for the System Polystyrene (1)+ Polystyrene (2)+ Methylcyclohexane. *J. Phys. Chem.* **1990**, *94*, 7943–7949.
- (31) Koningsveld, R.; Staverman, A. J. Liquid-Liquid Phase Separation in Multicomponent Polymer Solutions. I. Statement of the Problem and Description of Methods of Calculation. *J. Polym. Sci., Part A-2* **1968**, *6*, 305–323.
- (32) Koningsveld, R.; Staverman, A. J. Liquid-Liquid Phase Separation in Multicomponent Polymer Solutions. III. Cloud-Point Curves. *J. Polym. Sci., Part B: Polym. Phys.* **1968**, *6*, 349–366.
- (33) Solec, K. Cloud-Point Curves of Polymer Solutions. *Macromolecules* **1970**, *3*, 665–673.
- (34) Gualtieri, J. A.; Kincaid, J. M.; Morrison, G. Phase Equilibria in Polydisperse Fluids. *J. Chem. Phys.* **1982**, *77*, 521–536.
- (35) Qian, C.; Mumby, S. J.; Eichinger, B. E. Phase Diagrams of Binary Polymer Solutions and Blends. *Macromolecules* **1991**, *24*, 1655–1661.
- (36) Hu, Y.; Ying, X.; Wu, D. T.; Prausnitz, J. M. Liquid-Liquid Equilibria for Solutions of Polydisperse Polymers. Continuous

Thermodynamics for the Close-Packed Lattice Model. *Macromolecules* **1993**, *26*, 6817–6823.

(37) Hu, Y.; Ying, X.; Wu, D. T.; Prausnitz, J. M. Continuous Thermodynamics for Polydisperse Polymer Solutions. *Fluid Phase Equilib.* **1995**, *104*, 229–252.

(38) Ten Brinke, G.; Szeifer, I. Liquid-Liquid Phase Separation in Polydisperse Polymer Solutions: The Distribution Coefficient. *Macromolecules* **1995**, *28*, 5434–5439.

(39) Huang, C.; Olvera de La Cruz, M. The Early Stages of the Phase Separation Dynamics in Polydisperse Polymer Blends. *Macromolecules* **1994**, *27*, 4231–4241.

(40) Shrestha, R. S.; McDonald, R. C.; Greer, S. C. Molecular Weight Distributions of Polydisperse Polymers in Coexisting Liquid Phases. *J. Chem. Phys.* **2002**, *117*, 9037–9049.

(41) Evans, R. M. L.; Fairhurst, D. J.; Poon, W. C. K. Universal Law of Fractionation for Slightly Polydisperse Systems. *Phys. Rev. Lett.* **1998**, *81*, 1326.

(42) Xu, H.; Baus, M. Density Functional Theory of Phase Coexistence in Weakly Polydisperse Fluids. *Phys. Rev. E: Stat. Phys., Plasmas, Fluids, Relat. Interdiscip. Top.* **2000**, *61*, 3249.

(43) Stapleton, M. R.; Tildesley, D. J.; Quirke, N. Phase Equilibria in Polydisperse Fluids. *J. Chem. Phys.* **1990**, *92*, 4456–4467.

(44) Kristóf, T.; Liszi, J. Phase Coexistence and Critical Point Determination in Polydisperse Fluids. *Mol. Phys.* **2001**, *99*, 167–173.

(45) Wilding, N. B.; Sollich, P.; Fasolo, M.; Buzzacchi, M. Phase Behavior and Particle Size Cutoff Effects in Polydisperse Fluids. *J. Chem. Phys.* **2006**, *125*, 014908.

(46) Siepmann, J. I. A Method for the Direct Calculation of Chemical Potentials for Dense Chain Systems. *Mol. Phys.* **1990**, *70*, 1145–1158.

(47) Kumar, S. K.; Szeifer, I.; Panagiotopoulos, A. Z. Determination of the Chemical Potentials of Polymeric Systems from Monte Carlo Simulations. *Phys. Rev. Lett.* **1991**, *66*, 2935–2938.

(48) Mooij, G.; Frenkel, D.; Smit, B. Direct Simulation of Phase Equilibria of Chain Molecules. *J. Phys.: Condens. Matter* **1992**, *4*, L255–L259.

(49) de Pablo, J. J.; Laso, M.; Suter, U. W. Estimation of the Chemical Potential of Chain Molecules by Simulation. *J. Chem. Phys.* **1992**, *96*, 6157–6162.

(50) Karayiannis, N. C.; Mavrantzas, V. G.; Theodorou, D. N. A Novel Monte Carlo Scheme for the Rapid Equilibration of Atomistic Model Polymer Systems of Precisely Defined Molecular Architecture. *Phys. Rev. Lett.* **2002**, *88*, 105503.

(51) Wick, C. D.; Siepmann, J. I.; Theodorou, D. N. Microscopic Origins for the Favorable Solvation of Carbonate Ether Copolymers in CO₂. *J. Am. Chem. Soc.* **2005**, *127*, 12338–12342.

(52) Chen, B.; Siepmann, J. I. Partitioning of Alkane and Alcohol Solutes between Water and (Dry or Wet) 1-octanol. *J. Am. Chem. Soc.* **2000**, *122*, 6464–6467.

(53) Zhang, L.; Siepmann, J. I. Pressure Dependence of the Vapor–Liquid–Liquid Phase Behavior in Ternary Mixtures Consisting of *n*-Alkanes, *n*-Perfluoroalkanes, and Carbon Dioxide. *J. Phys. Chem. B* **2005**, *109*, 2911–2919.

(54) Rosch, T. W.; Errington, J. R. Investigation of the Phase Behavior of an Embedded Charge Protein Model through Molecular Simulation. *J. Phys. Chem. B* **2007**, *111*, 12591–12598.

(55) Shi, W.; Maginn, E. J. Continuous Fractional Component Monte Carlo: An Adaptive Biasing Method for Open System Atomistic Simulations. *J. Chem. Theory Comput.* **2007**, *3*, 1451–1463.

(56) Yoo, B.; Marin-Rimoldi, E.; Mullen, R. G.; Jusuf, A.; Maginn, E. J. Discrete Fractional Component Monte Carlo Simulation Study of Dilute Nonionic Surfactants at the Air–Water Interface. *Langmuir* **2017**, *33*, 9793–9802.

(57) Bai, P.; Siepmann, J. I. Gibbs Ensemble Monte Carlo Simulations for the Liquid–Liquid Phase Equilibria of Dipropylene Glycol Dimethyl Ether and Water: A Preliminary Report. *Fluid Phase Equilib.* **2011**, *310*, 11–18.

(58) Harwood, D. B.; Peters, C. J.; Siepmann, J. I. A Monte Carlo Simulation Study of the Liquid–Liquid Equilibria for Binary

Dodecane/ethanol and Ternary Dodecane/ethanol/water Mixtures. *Fluid Phase Equilib.* **2016**, *407*, 269–279.

(59) Panagiotopoulos, A. Z. Direct Determination of Phase Coexistence Properties of Fluids by Monte Carlo Simulation in a New Ensemble. *Mol. Phys.* **1987**, *61*, 813–826.

(60) Panagiotopoulos, A. Z.; Quirke, N.; Stapleton, M.; Tildesley, D. J. Phase Equilibria by Simulation in the Gibbs Ensemble: Alternative Derivation, Generalization and Application to Mixture and Membrane Equilibria. *Mol. Phys.* **1988**, *63*, 527–545.

(61) Zimm, B. H. The Scattering of Light and the Radial Distribution Function of High Polymer Solutions. *J. Chem. Phys.* **1948**, *16*, 1093–1099.

(62) Washburn, N. R.; Lodge, T. P.; Bates, F. S. Ternary Polymer Blends as Model Surfactant Systems. *J. Phys. Chem. B* **2000**, *104*, 6987–6997.

(63) Siepmann, J. I.; et al. Monte Carlo for Complex Chemical Systems—Minnesota, Version 17.1; Minneapolis, MN, 2017.

(64) Martin, M. G.; Siepmann, J. I. Novel Configurational-Bias Monte Carlo Method for Branched Molecules. Transferable Potentials for Phase Equilibria. 2. United-Atom Description of Branched Alkanes. *J. Phys. Chem. B* **1999**, *103*, 4508–4517.

(65) De Pablo, J. J.; Prausnitz, J. M. Phase Equilibria for Fluid Mixtures from Monte-Carlo Simulation. *Fluid Phase Equilib.* **1989**, *53*, 177–189.

(66) Martin, M. G.; Siepmann, J. I. Predicting Multicomponent Phase Equilibria and Free Energies of Transfer for Alkanes by Molecular Simulation. *J. Am. Chem. Soc.* **1997**, *119*, 8921–8924.

(67) Bai, P.; Siepmann, J. I. Selective Adsorption from Dilute Solutions: Gibbs Ensemble Monte Carlo Simulations. *Fluid Phase Equilib.* **2013**, *351*, 1–6.

(68) Chen, Q. P.; Xue, B.; Siepmann, J. I. Using the *k*-d Tree Data Structure to Accelerate Monte Carlo Simulations. *J. Chem. Theory Comput.* **2017**, *13*, 1556–1565.

(69) Allen, M. P.; Tildesley, D. J. *Computer Simulation of Liquids*; Clarendon Press: Oxford, 1987.

(70) Wick, C. D.; Siepmann, J. I. Self-Adapting Fixed-End-Point Configurational-Bias Monte Carlo Method for the Regrowth of Interior Segments of Chain Molecules with Strong Intramolecular Interactions. *Macromolecules* **2000**, *33*, 7207–7218.

(71) Martin, M. G.; Siepmann, J. I. Transferable Potentials for Phase Equilibria. 1. United-Atom Description of *n*-Alkanes. *J. Phys. Chem. B* **1998**, *102*, 2569–2577.

(72) Stubbs, J. M.; Potoff, J. J.; Siepmann, J. I. Transferable Potentials for Phase Equilibria. 6. United-Atom Description for Ethers, Glycols, Ketones, and Aldehydes. *J. Phys. Chem. B* **2004**, *108*, 17596–17605.

(73) Maitland, G. C.; Rigby, M.; Smith, E. B.; Wakeham, W. A. *Intermolecular Forces: Their Origin and Determination*; Oxford University Press: 1981.

(74) Wood, W. W.; Parker, F. R. Monte Carlo Equation of State of Molecules Interacting with the Lennard-Jones Potential. I. A Supercritical Isotherm at about Twice the Critical Temperature. *J. Chem. Phys.* **1957**, *27*, 720–733.

(75) Sun, L.; Siepmann, J. I.; Schure, M. R. Conformation and Solvation Structure for An Isolated *n*-Octadecane Chain in Water, Methanol, and Their Mixtures. *J. Phys. Chem. B* **2006**, *110*, 10519–10525.

(76) Treszczanowicz, T.; Cieślak, D. (Liquid + liquid) Equilibria in (a Dimethyl Ether of a Polyethylene Glycol + an *n*-Alkane). *J. Chem. Thermodyn.* **1993**, *25*, 661–665.

(77) Du, X.; Sun, Z.; An, L. Effect of Chain-Length Dependence of Interaction Parameter on Spinodals for Polydisperse Polymer Blends. *Macromol. Theory Simul.* **2006**, *15*, 440–445.

(78) Chen, J. L.; Xue, B.; Harwood, D. B.; Chen, Q. P.; Peters, C. J.; Siepmann, J. I. A Monte Carlo Simulation Study of the Interfacial Tension for Water/oil Mixtures at Elevated Temperatures and Pressures: Water/*n*-dodecane, Water/toluene, and Water/(*n*-dodecane + toluene). *Fluid Phase Equilib.* **2017**, DOI: 10.1016/j.fluid.2017.06.015.

- (79) White, R. P.; Lipson, J. E. G.; Higgins, J. S. New Correlations in Polymer Blend Miscibility. *Macromolecules* **2012**, *45*, 1076–1084.
- (80) Šolc, K. Multiphase Equilibria in Solutions of Polydisperse Homopolymers. I. Three-Phase Equilibria in Ternary and Quasiternary Systems. *J. Polym. Sci., Polym. Phys. Ed.* **1982**, *20*, 1947–1961.
- (81) Hsu, C. C.; Prausnitz, J. M. Thermodynamics of Polymer Compatibility in Ternary Systems. *Macromolecules* **1974**, *7*, 320–324.
- (82) Ben-Naim, A.; Marcus, Y. Solvation Thermodynamics of Nonionic Solutes. *J. Chem. Phys.* **1984**, *81*, 2016–2027.
- (83) Kurata, M. *Thermodynamics of Polymer Solutions*; CRC Press: 1982.
- (84) Maranas, J. K.; Kumar, S. K.; Debenedetti, P. G.; Graessley, W. W.; Mondello, M.; Grest, G. S. Liquid Structure, Thermodynamics, and Mixing Behavior of Saturated Hydrocarbon Polymers. 2. Pair Distribution Functions and the Regularity of Mixing. *Macromolecules* **1998**, *31*, 6998–7002.
- (85) McCarty, J.; Guenza, M. G. Multiscale Modeling of Binary Polymer Mixtures: Scale Bridging in the Athermal and Thermal Regime. *J. Chem. Phys.* **2010**, *133*, 094904.
- (86) Medapuram, P.; Glaser, J.; Morse, D. C. Universal Phenomenology of Symmetric Diblock Copolymers near the Order–Disorder Transition. *Macromolecules* **2015**, *48*, 819–839.
- (87) Radlauer, M. R.; Sinturel, C.; Asai, Y.; Arora, A.; Bates, F. S.; Dorfman, K. D.; Hillmyer, M. A. Morphological Consequences of Frustration in ABC Triblock Polymers. *Macromolecules* **2017**, *50*, 446–458.
- (88) Mao, S.; MacPherson, Q.; Spakowitz, A. J. Fluctuation Effects in Semiflexible Diblock Copolymers. *ACS Macro Lett.* **2018**, *7*, 59–64.